Version of Record: https://www.sciencedirect.com/science/article/pii/S0022311521004712
Manuscript_1da932250ffb13e69154211179113891

Characterization of the molten salt FMgNaK through ab initio molecular dynamics and experimental density measurements

Andrew Russell Solano[a], solanoanddragon@gmail.com

Austin Clark[a], austin.david.clark@gmail.com

Kent P. Detrick[a], kent.detrick@gmail.com

Matthew J. Memmott[a], memmott@byu.edu

Stella D. Nickerson[a], stelladn@byu.edu, corresponding author

[a]Brigham Young University, Provo, UT 84602

Abstract: The selection of a salt species for use in a molten salt reactor MSR is a key part of any MSR design. However, many salts have sparse or no thermophysical property data sets, especially those with higher melting points. One such salt is the eutectic mixture of $(NaF)_{0.345}(KF)_{0.59}(MgF_2)_{0.065}$, or FMgNaK, and is explored here through ab initio molecular dynamics (AIMD) simulation (1023-1273K) as well as experimental measurement of the liquid density using the Archimedean method (973-1223K). Predicted densities from AIMD are similar to experimentally-measured densities, though with more noise, suggesting that the small scale necessitated by AIMD simulations may be problematic for simulating FMgNaK in particular. The coefficient of thermal expansion is predicted from simulation, and salt structure is characterized. Mg-F-Mg chaining is observed in the salt network, though the low concentration of Mg inhibits chaining on the scale that is observed in $(LiF)_{0.67}(BeF_2)_{0.33}$, or FLiBe.

Keywords: molten salt, FMgNaK, ab initio molecular dynamics, structure

1. Introduction

While several eutectic mixtures of halide salts have been considered as coolants for molten salt reactors (MSRs)[1], one salt that has received relatively little attention is $(NaF)_{0.345}(KF)_{0.59}(MgF_2)_{0.065}$, or (FMgNaK). FMgNaK poses an economical alternative to the expensive purification process of FLiBe[2], or $(LiF)_{0.67}(BeF2)_{0.33}$, which is the most common[1] salt used in MSR designs. FMgNaK has comparable heat capacity, thermal conductivity, and neutron absorption[3] without intense ^{7}Li-enrichment, which added $10,000/kg to the cost of FLiBe in 2012[2]. Indeed, ^{7}Li-enrichment is needed for many molten salt alternatives (FLiBe, FLiNaK, LiF, KLiCl) as natural lithium produces tritium, which permeates through the reactor, severely harming both the reactor and the environment[4, 5]. ^{6}Li also has a large neutron absorption cross-section, making it a significant neutron poison[6]. FMgNaK, however, does not require any lithium, making the salt less expensive, less poisonous to neutronics, and safer to produce in large quantities. Handling beryllium is also very dangerous. Acute skin exposure or inhalation can quickly cause chemical pneumonia, lung diseases, and even lung cancer, among many other ailments[7]. On the other hand, while personal protective equipment is still required to handle FMgNaK, none of its components are highly toxic and none are suspected carcinogens[8-11]. Additionally, in a neutronic analysis of thermal diffusion length and fermi age, the components of FMgNaK rival the components of FLiBe, having excellent neutronic properties[3].

Despite these advantages, FMgNaK has not traditionally been considered for MSR designs as salt temperatures for early reactors only reached a maximum of between 720-750 °C[12]: just barely above FMgNaK's eutectic melting point of 685 °C[13]. However, improvements in material science and fabrication techniques enable modern reactors to reach much higher temperatures, bringing the salt back into the limelight[14]. Still, because FMgNaK has been overlooked for so long, its properties are even less well-characterized than other salts, with no entry in even large, inclusive databases of molten salt properties[15].

This paper describes (AIMD) simulations used to predict both thermophysical properties of FMgNaK (density, coefficient of thermal expansion), and its structure. AIMD has been used to study several molten fluoride salts including $(LiF)_{0.465}(NaF)_{0.115}(KF)_{0.42}$ (FLiNaK), and FLiBe[16-24]. AIMD simulations of FLiNaK from our own lab were found to predict salt structure very well compared to pair distribution functions generated by neutron scattering experiments[16]. (That study also predicted salt density very closely in line with one established experimental correlation, though it fit other correlations from the literature less closely). AIMD also has the advantage of not requiring an interatomic potential model, unlike classical molecular dynamics, which is helpful for a little-studied material like FMgNaK which does not have established potentials. FMgNaK density was also experimentally measured using the Archimedean method, generating some of the first experimental data ever published on this intriguing salt, and experimental density was compared to predictions from simulation.

2. Methodology

2.1. Simulation methods

2.1.1. Simulation setup

We created a simulation cell for each of 20 AIMD production runs. Each cell contains 95 atoms with a eutectic composition of NaF-KF-MgF_2 (49 F atoms, 3 Mg atoms, 16 Na atoms, and 27 K atoms). Initial configurations of atoms were generated at random using the Packmol software package[25, 26]. The average box size of our equilibrated simulations was 12.72 ± .065 Å, with the error representing a 95% confidence interval on the mean.

We performed AIMD simulations using the CP2K software[27, 28]. These simulations were based on density functional theory (DFT), and utilized the Perdew-Burke-Ernzerhof (PBE) exchange-correlational functional[29], which is a form of the generalized gradient approximation (GGA). We employed the Gaussian and plane waves method (GPW) to approximate the wavefunctions and electron density[30-32]. All atoms were modelled using DZVP-MOLOPT-SR-GTH basis sets[33, 34], and all core electrons were treated with GTH pseudopotentials[27, 34-36]. A detailed explanation of our AIMD methodology is also given by Frandsen et al., and was found to accurately predict molten salt density compared to experimental correlations from the literature and structure FLiNaK compared to neutron scattering data[16]. The main difference between methodology described in that publication and the work described here is the values of the GPW cutoffs used: this work uses 2500 Ry for the plane-wave energy cutoff, and 200 Ry for the relative cutoff (the plane-wave cutoff of the reference grid upon which the gaussians are mapped). These cutoffs were set higher here than in that previous paper, which in general should increase accuracy.

The temperature was controlled using the canonical sampling through velocity rescaling[37] (CSVR) thermostat, which is purported to be more ergodic than the Nosé-Hoover thermostat[37]. The system barostat also employed canonical sampling through velocity rescaling. We simulated FMgNaK over the temperature range 750-1000 °C. We used the NPT ensemble with an external pressure of 1 atm and a timestep of 0.5 fs. We allowed the simulations to equilibrate for 20 ps and obtained our equilibrium properties by averaging the following 20 ps of the simulation, a technique successfully employed by Caro et al[38].

Van der Waals dispersion corrections were not included in our simulations, as literature suggests these interactions only play a significant role in larger boxes[39, 40], defined by Shi et. al. as simulations greater than 1024 atoms[39]. Our simulation size of 95 atoms suggests Van der Walls forces are negligible in comparison to electrostatic interactions, and similar salt systems have accurately predicted salt behavior without Van der Waals forces[16]. In our results section below we compare our simulated density with experimental density measurements and further confirm our simulations can model the behavior of FMgNaK with reasonable accuracy without including Van der Waals forces.

2.1.2. Density and equilibration

The density of a simulated molten salt is quite sensitive to the interaction energies of a system,[23] and so an accurate density prediction is a reasonably good indication that simulated energies are adequate to describe the behavior of a molten salt system. Density is calculated straightforwardly from the NPT ensemble, taking:

$$\rho = \frac{m}{V(T)} \qquad (1)$$

where m is the total mass of all particles in a cell and V(T) is the equilibrium volume as a function of temperature. Density of molten salts at this temperature range has traditionally been fit to a simple linear regression for a wide range of fluoride salts[41-44]. A D-optimal design of experiment for a simple linear regression mandates that the variance be minimized for the two extreme points of the range being investigated. In our case this means that the highest and lowest temperatures simulated carry more information about the density than any other two temperatures within the range simulated. Our 20 simulations were thus weighted towards either end of the temperature range of interest.

To verify that the liquid density is indeed a linear function of temperature over the range investigated, and to allow for regression of other properties of interest, several intermediate temperatures were also simulated. The number of simulation cells at each temperature simulated is given in Table 1.

Table 1: A list of the simulated temperatures and the number of simulations conducted at each temperature.

Temperature (°C)	Quantity
750	6
800	2
850	2
900	2
950	2
1000	6

We checked for equilibration by testing if the average density over a period of 5 ps (10,000 steps) in the production run was within 2% of the average density of the subsequent 5 ps of that production run. If a production run failed to meet this condition throughout its data range, the run was defined as unequilibrated and not used in calculations. See Section 3.0 for information on the impact of this definition on our results.

2.1.3. Coefficient of thermal expansion

From the temperature dependency of our density measurements, we calculated the coefficient of thermal expansion (CTE; α) using Eq. (2).

$$\alpha \equiv \frac{1}{V}\left(\frac{dV}{dT}\right)\bigg|_P = -\frac{1}{\rho}\left(\frac{d\rho}{dT}\right)\bigg|_P \qquad (2)$$

where T is the temperature, ρ is the density, and V is the volume. This technique has been successfully used to calculate CTE in literature[18] and is an accurate method of determining thermal expansion in liquids. Our density simulations are also directly compared to experimental measurements, making properties directly derived from density similarly verifiable.

2.1.4. Radial distribution function

Radial distribution functions (RDFs) contain valuable information about the structure of a material, especially within the first peak. The normalized height of the first peaks in the RDFs correspond to the relative strength of the interaction between the ions, and the x-axis coordinate value of each first peak indicates the most probable radial distance between an ion of species a and another ion of species b within its solvation shell. The normalized integral of the RDF up to the terminus of the first peak yields the average coordination number of species b with respect to species a. We determined first-shell coordination numbers by integrating the RDF from zero to its first minimum. RDF's were generated for each of our equilibrated simulations.

RDFs were generated from the CP2K-generated trajectory files using the Visual Molecular Dynamics (VMD) software package[45] and these RDFs incorporate periodic boundary conditions (PBC). RDFs are used to determine the structure and potential speciation of the ions in FMgNaK.

2.2. Experimental methods

To prepare FMgNaK salt, we first purchased the component salts KF, NaF, and MgF_2 from Sigma Aldrich at 99.99% purity. Salts were stored and handled exclusively within an argon glovebox, which is also where all experimental measurements were conducted. We dried each salt in a dry box at 500 °C for twenty-four hours, after which we weighed and mixed each salt in order to produce molar ratios of $(NaF)_{0.345}(KF)_{0.59}(MgF2)_{0.065}$. We then melted and mixed the solid powder mixture at 700 °C.

Any water contamination before or after drying would lead to corrosion of the container material[46]; therefore, after density measurements were taken, a semiquantitative inductively coupled plasma mass spectrometry (ICP-MS) analysis was performed on our salt mixture. This semiquantitative analysis gives an order of magnitude estimate of the concentration of corrosion metals in the salt. In our samples, the presence of Ni, Cr, and Fe were detected, all at concentrations at two orders of magnitude lower than K, Na, and Mg. From this, we used the molar volume additivity model to estimate the maximum effect of these contaminants on the density of the salt. Taking the molar volumes of NiF_2, CrF_2, and FeF_2 as 32 $\frac{cm^3}{mole}$, to be conservative, the maximum change in density of our salt samples due to contaminants is estimated as 0.2%.

We built a density measurement device, shown in Figure 1, that operates on the Archimedean method, a robust and relatively simple method[47] which has previously been used to measure the density of molten salts by, among others, researchers at Sandia National Laboratory who documented their experimental setup in great detail[48]. In this method, a bob of known volume is submerged in a liquid, and the buoyancy force measured on the bob is used to calculate liquid density according to:

$$\rho = \frac{F_b}{g \cdot V(T)} \qquad (3)$$

where ρ is density, F_b is the buoyancy force, g is the gravitational constant, and $V(T)$ is the volume of the bob at the salt temperature.

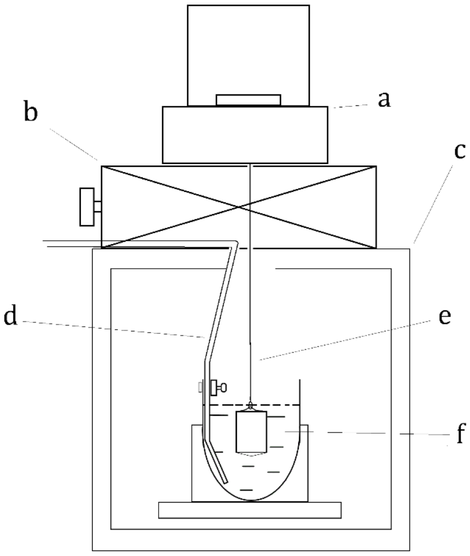

Figure 1: BYU Molten Salt Laboratory Archimedean method density apparatus diagram. a – Mettler Toledo analytical scale with hook for mass underneath: model ML503T or MS303TS, b – stainless steel heavy duty scissor lift, c – Paragon SC-2 Pro Furnace with Orton SntryXpress 5.0 Controller, d – Omega Industry Type-K thermocouple, e – nickel wire, f – nickel bob.

In order to measure buoyancy force, the bob is suspended from a hook on a wire connected to an analytical scale, which measures wire tension. Commonly, the difference in tension when the bob is suspended in atmosphere (in our case argon) and in the liquid is assumed to be equivalent to the buoyancy force on the bob in the liquid; here, we have added corrections for the buoyancy force on the bob in argon and for the force from surface tension on the wire as it crosses through the salt surface, giving the following expression for salt density:

$$\rho_{salt} = \frac{F_0 - F_1 + \frac{M_{Ar}P}{RT_0} gV_{probe}(T_0) + 2\gamma\pi D_{wire}}{gV_{probe}(T_1)} \quad (4)$$

where the F_0 is the measured tension force of the probe in atmosphere (in our case Ar at room temperature), F_1 is the measured tension force when the bob is submerged in the salt, M_{Ar} is the molar mass of Ar, P and T_0 are the pressure and temperature of the ambient Ar, $V_{probe}(T_1)$ is the volume of the probe at the salt temperature, γ is the interfacial tension between Ar and the salt, and D_{wire} is the diameter of the wire. The expression for surface tension force ($2\gamma\pi D_{wire}$) assumes a contact angle of 180° between the wire and the salt surface, and is taken to act *downward* on the wire given that *upward* wicking of the salt on the bob was consistently observed. The 2 is included because the wire breaks the surface of the salt at two different points. The surface tension of FMgNaK has not been characterized in the literature, and so our calculation use the surface tension of (NaF)0.4(KF0.6)[43], a salt with a very similar composition.

In our apparatus, nickel was chosen as the bob material due to its low reactivity with highly oxidative fluoride salts[49]. All materials directly in contact with the molten salt are made of pure nickel except the Type-K thermocouple sheath, which is made of a resistant nickel alloy which has previously been used in studies of molten fluoride salts[50]. Bob volume was determined by performing a measurement on 18-ohm resistant water at room temperature, then solving Eq. 4 for bob volume using the known density of water. The volume of the bob when submerged in the salt was adjusted to account for elevated salt temperature using an empirical expression for thermal expansion of nickel from Abdullaev et al.[51].

FMgNaK density was measured at five temperatures: T= 700, 750, 800, 850, 900, and 950 °C. Measurements were taken at each of those six temperatures in a random order. Then, the wire was replaced, and the measurements were taken at the same six temperatures in a different random order. This was repeated until there were three replicates at each temperature. Randomizing temperature order like this is done because salt vapors can deposit on the wire, increasing tension, which leads to an artificially low measured salt density. Salt vapor deposition increases with salt temperature (which increases vaporization), but also builds up over time. Randomizing the order of temperatures at which measurements are taken removes time as a confounding variable when determining the dependance of density on temperatue[52]. However, no salt deposition was visible on the wire at any point during our measurements.

The apparatus and method were checked by measuring the density of $(NaNO_3)_{0.3592}(KNO_3)_{0.6408}$ (solar salt), as detailed in Appendix A. From this, we concluded that our measured densities for solar salt are well in accordance with the literature, and that the corrections for surface tension and the buoyancy force on the bob in atmosphere are significant, though small.

3. Results and discussion

3.0 Note on simulation equilibration

Nineteen of our twenty simulations equilibrated in the allotted timeframe, however one simulation at 850 °C was not equilibrated at the end of our 40 ps simulation period. This simulation was not used in our analysis. Due to this issue, the diffusion coefficient values for 850 °C will not have error bars.

3.1 Density

There is little experimental literature on the properties of FMgNaK, including relatively straightforward properties such as density. Addressing this lack, we present an experimental correlation for FMgNaK density using techniques described in Section 2.2 above. We used this correlation to benchmark our AIMD densities. We compare our experimental and simulation densities to an additive molar volume estimate for the mixture based upon the densities of the binary salt components, MgF_2, NaF, and KF over the range of temperatures explored. The calculation of the additive density model is described in Appendix B. This method has been found to agree well with experimentally measured densities in fluoride salts[13, 41, 42]. We compare simulation and experimental densities, as well as these additive volume density estimates across our temperature range, in Figure 2.

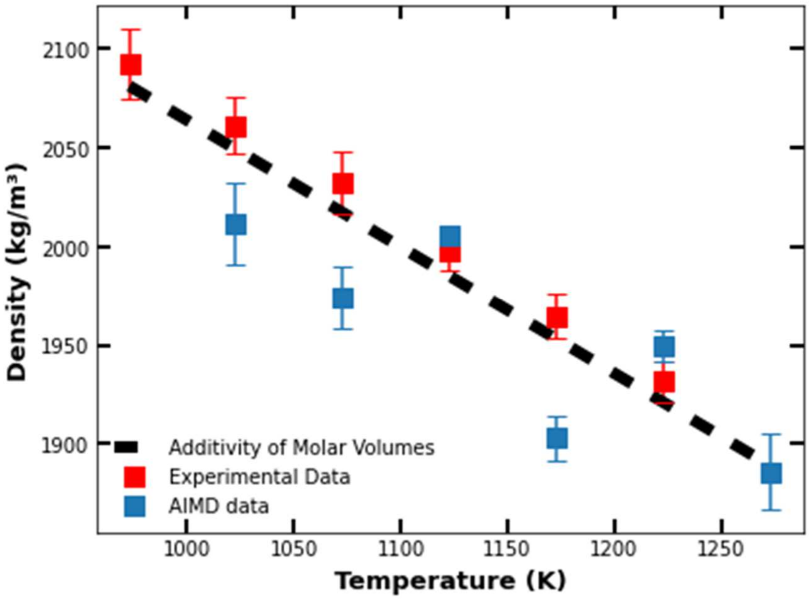

Figure 2: Density measurements of FMgNaK as a function of temperature. Error bars represent one sigma standard deviation on the mean. Each of the experimental density data points represents 3 replicates. For the simulation data, 6 parallel simulations were performed at the lowest (750°C) and highest (1000°C) temperatures,, while only 2 parallel simulations were performed at temperatures in the middle of that range (this was done in hopes of producing a better linear fit, as described in Section 2.1.1.) One simulation cell, at 850°C, never equilibrated according to our criteria as laid out in Section 2.1.2., and so was not included. The simulation data point at that temperature therefore has no error bar.

The linear fits for FMgNaK density shown in Figure 2 are listed in Table 2 and used in Eq. (3)

$$\rho\left[\frac{kg}{m^3}\right] = \mathrm{a}\cdot T[\mathrm{K}] + \mathrm{b} \qquad (3)$$

Table 2: Coefficients of the linear density models. The additive model was calculated from a molar weighted average of molar volumes for KF, MgF_2, and NaF from Cantor et. al.[53].

Model	a (kg/m^3-K)	b (kg/m^3)	Range (K)
Experimental	-0.6578	2734	973-1273
Simulated	-0.4810	2502	1023-1273
Additive	-0.6318	2711	973-1273

where ρ is the density, and T is the temperature in Kelvin. As shown in Figure 2, both experimental and AIMD density values are relatively close to that predicted by the additivity model, and both follow the expected trend of decreasing density with increasing temperature. However, the experimental values follow a linear relationship more tightly, while the AIMD values exhibit more noise, and from Table 2, the slope of the linear fit to the simulation data diverges from that of the linear fit of the experimental data as well as the additive model. However, note that the range of densities calculated from simulation overlaps with the linear trend of the experimental data.

AIMD simulation studies of molten salts are somewhat rare, and only a few report salt density as a function of temperature. In addition to our previous study on FLiNaK[16], we found three papers that did so: two on KLiCL[18, 54] and one on FLiNak and FLiBe[55]. None of these included newly-performed density measurements of the sort reported here; rather they compared simulated densities to established experimental correlations from the literature. All seem to show similar results: simulated density trends close to the experimental correlations, but with different slopes (we did find near-perfect agreement with one out of four published experimental correlations of FLiNaK[16]). Of these four studies, only the Bengston et al paper on KLiCl[18] presented individual experimental data points from the literature, rather than simply the linear correlation model, and that paper only included two simulated temperatures for KLiCl. Consequently, our data as shown in Figure 2 show the relative noise of AIMD-generated and experimental molten salt densities in a way previous studies have not. This may suggest *why* AIMD studies consistently predict densities close to experimental correlations but with different linear fits: it is a consequence of the noise created by the relatively small scale of these simulations. Indeed, larger-scale classical molecular dynamics simulations of molten salts seem to predict density trends more aligned with established experimental correlations[23]. We conclude that the precise linear fits of density reported from molten salt AIMD studies, including those mentioned above, should not be taken as reliable, though general agreement in magnitude and direction with experimentally-determined density trends may still suggest that simulations are capturing the basic structural behavior of these salts.

3.2 Coefficient of thermal expansion

The coefficient of thermal expansion (CTE) for FMgNaK was calculated using densities throughout our temperature range as described in Section 2. The slope of the line fitted to all our CTE values was 6.09×10^{-8} K^{-2}, and our values had a range of 1.60×10^{-5} K^{-1}, suggesting negligible temperature dependence. The reported CTE value was calculated at 800 °C and averaged between our two simulations at that temperature. In the absence of an experimentally determined CTE value for FMgNaK, we validate our value using the molar-weighted average CTE of NaF, KF, and MgF_2. NaF, KF, and MgF_2, were measured at 1122 °C, 965 °C, and 1417 °C, respectively[56]. This resulted in an approximated CTE of 3.27 K^{-1}. However, it should be noted that the CTE is dependent on structure, which will change when these salts are mixed, so this average is intended merely as a general estimate to benchmark our values. Our simulations reported a CTE of $2.46 \pm .070$ ($K^{-1} \times 10^{-4}$), where the error bounds represent a 95% confidence interval.

In general, CTE values from AIMD simulations have consistently been reported as lower than those found in experimental measurements[57]. This caused an approximate downward shift of as much as 1.0×10^{-4} K^{-1} in one study of the CTE of FLiNaK[18]. Our findings agree with the simulation shift suggested by Woodward et al.[57] and Nam et al.[18]

3.3 Structural information

The structural data for FMgNaK is summarized in

Table 3, Table 4, and Figures 3-7. AIMD simulation values for FMgNaK's average bond length (first-peak radius), coordination number, and first peak height are compared with experimental values of FLiNaK due to a similar chemical makeup and to compare the effects of MgF_2 and LiF. Structural properties of FMgNaK are also compared with the properties of FMgNaK's binary components (MgF_2, NaF, and KF) to compare structural changes that occur as a result of combining the binary components.

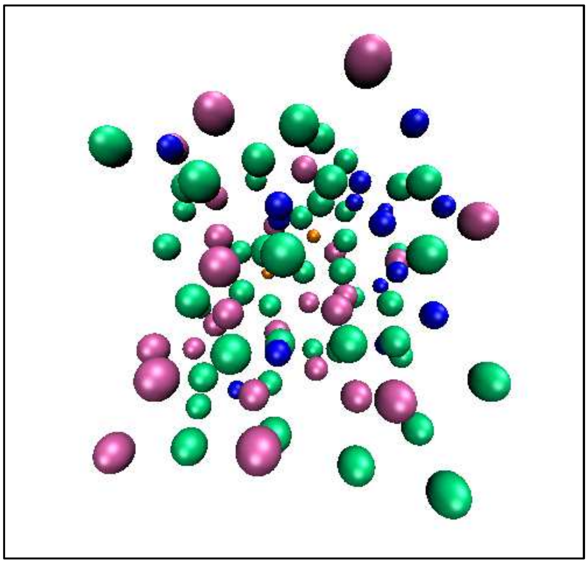

Figure 3: Snapshot of AIMD trajectory for FMgNaK at 1073 °C. Colors green, orange, blue, and purple correspond to elements F, Mg, Na, and K, respectively.

95% confidence intervals for structural values across our temperature range deviated by less than 2%, suggesting negligible structural temperature dependence.

Table 3 reports the average values of our simulations at 1000 °C.

3.3.1 FMgNaK compared to binary salts

Compared to FMgNaK's constituent binary salts, FMgNaK's coordination number for Na-F increases, yet this increase is less than the increase for K-F. However, the first-peak radius of Mg-F, Na-F, and K-F remained within 5% of the binary salt experimental values[58]. The coordination number likely increased less in Na-F than K-F because Na^+ ions are more electronegative than K^+ ions[59]. While Mg^{2+} ions are even more electronegative than Na^+ ions[59], the ratio of anion to cation in FMgNaK (49:46) is *much* lower than the ratio in pure MgF_2 (2:1), so the Mg-F coordination in pure MgF_2 is likely higher than observed in FMgNaK.

3.3.2 FMgNaK compared to FLiNaK

First peak radius and coordination numbers for FMgNaK were compared to those calculated for FLiNaK in a previous AIMD study (which was found to predict neutron scattering data very well, suggest accurate structure predictions) [16]. The absence of Li is an advantage of FMgNaK compared to FLiNaK, but it also alters the structure of the salt. The Mg^+-F^- pair in FMgNaK has a wider peak radius and larger coordination number than the Li^+-F^- pair in FLiNaK, suggesting more F anions gathering around Mg^{2+} in a wider coordination shell. This in turn may explain why the F-F pair in FMgNaK has a significantly smaller first peak radius and larger coordination number than the F-F pair in FLiNaK—the F^- in FMgNaK are more concentrated around the Mg^{2+} ion, bringing them closer to each other in general. Recent work suggests that these the different chemical environments around F^- in different fluoride molten salts will affect the thermodynamics salt solutions, and needs to be taken into account in order to e.g. predict electrochemical potentials in salt electrolytes[60]; future studies more directly relating the different coordination of F^- in FMgNaK and FLiNaK to different thermodynamics would be of interest. (Na-F and K-F first-peak radii remained relatively unchanged between FMgNaK and FLiNaK.)

Table 3: Comparison between the first-peak radius and coordination number found in our AIMD simulations at 800 °C with those found experimentally in similar salts. We should note that all experimental values for binary salts are the same as those cited by Nam et al in their simulation study of FLiNaK and FLiBe.[55] *.*

Ion Pair	First-peak height of FMgNaK (AIMD)	First-peak radius (Å)			Coordination Number		
		FMgNaK (AIMD)	Binary Salts (Lit.)	FLiNaK (Previous Study)	FMgNaK (AIMD)	Binary Salts (Lit.)	FLiNaK (Previous Study)
Mg^{2+}–F^{-}	11.7	1.95	–*	–	5.25	–*	–
Na^{+}–F^{-}	4.64	2.25	2.30[b]	2.20[a]	5.24	4.1[b]	5.42[a]
K^{+}–F^{-}	3.20	2.55	2.6[b]	2.60[a]	6.11	4.9[b]	7.12[a]
F^{-} – F^{-}	1.55	3.55	–	3.10[a]	16.5	–	11.2[a]
Li^{+} – F^{-}	–	–	1.85[b]	1.84[a]	–	3.7[b]	4.0[a]
Mg^{2+}–Mg^{2+}	4.17	3.45	–	–	0.66	–	–

[a] Data for FLiNaK from our previous AIMD study, which was well-validated by neutron diffraction experiment [16]

[b] Experimental data for binary salts from Ohno et al.[58]

* We were unable to find literature values for coordination numbers or first peak radii of MgF$_2$.

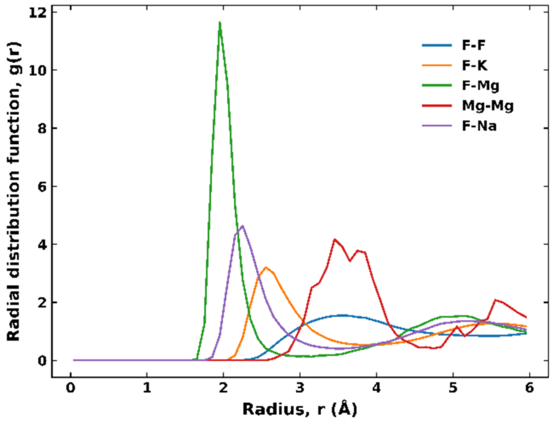

Figure 4: Radial distribution functions (RDF) of FMgNaK at 800 °C. This analysis was performed on each of our simulations to check for temperature dependence, and variance across temperatures was minimal.

3.3.3 Magnesium Chaining

In studies of FLiBe, Be-F chaining had a significant influence on transport properties, causing viscosity to increase sharply as the concentration of Be^{2+} ions increases[22]; this has important implications since the eutectic composition of molten salts is typically chosen for the lowest possible operating temperature, but FLiBe's eutectic composition is undesirable due to the effect of beryllium chaining on viscosity, and alternate compositions or network-breaking cations must be employed to counteract this effect in FLiBe. As far as we can determine, the effect of such chaining on molten salt density has not been discussed in the literature, though given that we found FMgNaK density to be fairly close to that predicted by a simple additive model, we doubt chaining has a significant effect. Though this work does not look at transport properties, we believe the presence (or absence) of magnesium chaining in FMgNaK would be of interest to the community and a starting point for future work, and so examined our results for this phenomenon.

Mg–Mg distances below 4.0 Å were used to classify chaining events. This cutoff was chosen because it is approximately the distance of 2 Mg-F bonds and a similar distinction was used in defining beryllium chaining in FLiBe[22]. This made chained magnesium easily distinguishable from unchained magnesium, which consistently had a Mg–Mg distance of at least 5.0 Å.

We observed Mg-F-Mg chaining in 52.6% of our simulations, suggesting the effect of Be-F-Be chaining in FLiBe may also occur in FMgNaK with Mg. As shown in Figure 5, the Mg of simulation index 47 (Mg_{47}) and Mg_{48} remained closely bonded to F_{32} from 15 ps until 27 ps. In this simulation at 800 °C, F_{32}–Mg_{47} and F_{32}–Mg_{48} bonds were 2.11 Å and 2.20 Å, respectively. The distance between Mg_{47} and Mg_{48} was 3.43 Å, well below two Mg-F bond lengths, suggesting that the chaining does not occur linearly. Indeed a visual inspection of the chaining events observed in all equilibrated simulations shows octahedral Mg-F complexes sharing three F^- ions, as shown in Figure 6. This suggests that the chaining occurs along an octahedral face, and not an edge or a vertex of the octahedral.

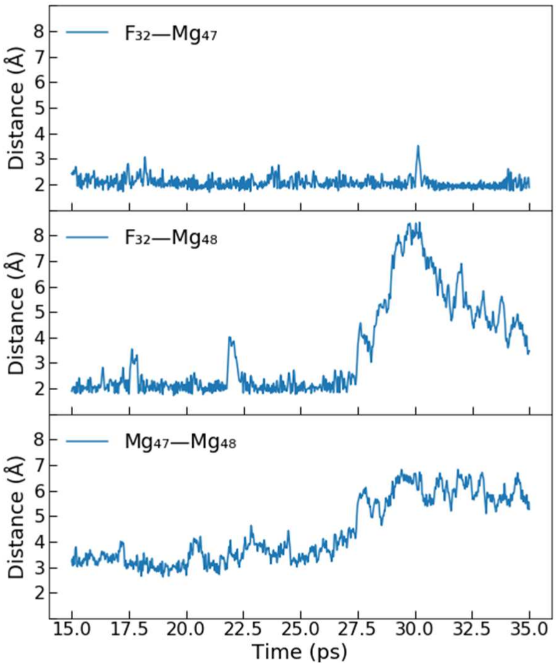

Figure 5: Distances between 3 ions involved in Mg-F chaining in FMgNaK at 800 °C. The figure only displays the period within a data range of 15-35 ps.

After sharing F_{32} for over 12 ps, the distances between F_{32}–Mg_{48} and Mg_{47}–Mg_{48} dramatically increased at 27 ps. These finding suggest that Mg-F-Mg chaining occurred between two of the Mg^{2+} ions, and at 27 ps Mg_{48} separated from F_{32}, breaking the chaining event.

From simulations at this scale, it is difficult to conclude whether chaining would have a significant effect on FMgNaK viscosity, suggesting that future studies utilizing larger-scale simulations that can more reliably predict transport properties would be desirable. However, the repeated formation of Mg-F-Mg complexes in our simulations suggest that Mg^{2+} has a strong preference for speciation with other Mg^{2+} ions, and so at higher concentrations of MgF_2, MgF_2-NaF-KF salts would undergo significant chaining.

Similar Mg–F–Mg chaining occurred in 10 out of our 19 equilibrated simulations. The distribution of these potential chaining events across our sample temperatures is given in Table 4. No chain involving 3 Mg^{2+} ions was observed in any simulation.

Table 4: Equilibrated simulations that contained chaining events.

Temperature (K)	Fraction of Simulations with Chaining	Average Mg–Mg distance (Å) in Chain
1023	33.3%	3.45
1073	100%	3.50
1123	100%	3.25
1173	0%	–
1223	50%	3.45
1273	66.7%	3.58

In FLiBe, the beryllium chaining occurs with negligible impact to the F^- coordination of Be^{2+}. In FMgNaK, the F^- coordination of Mg^{2+} appears to shift. In unchained magnesium ions, the fluoride coordination appears to typically be five, and is structured as shown in Figure 6. However, in a magnesium chaining event, the fluoride coordination is consistently six, as shown in Figure 7.

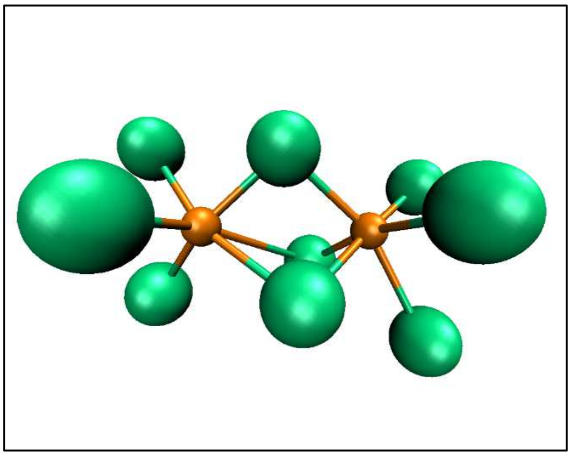

Figure 6: An example of Mg-F chaining observed at 750 ℃. The third Mg^{2+} ion, Mg_{92}, was completely dissociated and did not participate in Mg-F chaining.

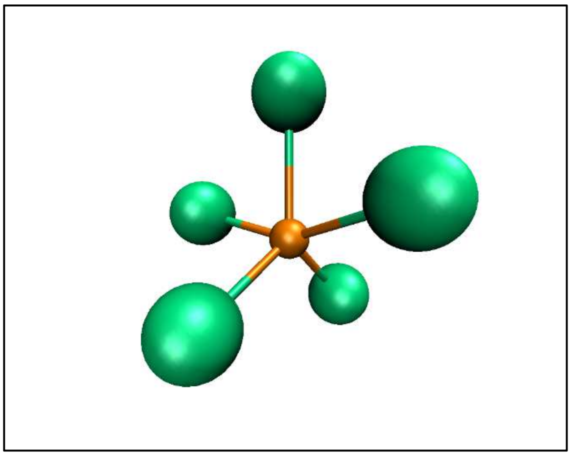

Figure 7: An example of a Mg monomer, observed in FMgNaK at 750 °C. It should be noted the simulation used in this figure is a separate simulation than that of Figure 6, though both were performed at 750 °C.

4. Conclusions

In this work, we employed AIMD simulations to predict structure and properties of FMgNaK. Density was also measured experimentally, providing some of the first experimental data publicly available on this salt. Density predicted by AIMD agreed well with experimental density by the standards of molten salt AIMD studies, but were noisy and did not follow a linear relationship as tightly as the experimentally-measured densities; larger-scale simulations (likely employing classical molecular dynamics) might remedy this. FMgNaK structure in the simulated salt was characterized through radial distribution functions and coordination numbers. Within this structure, we observed Mg-F chaining similar to the Be-F chaining known to occur in FLiBe molten salt and to have an important effect on salt viscosity, and suggests that future work explore the effect of increasing Mg concentrations on salt structure and properties, particularly transport properties, would be of value.

Data Availability

The raw or analyzed data reported in this study is available upon request.

Declaration of Competing Interest

This work and the manuscript present no conflicts of interest.

Credit authorship contribution statement

Andrew Solano: Methodology, Software, Data Curation, Validation, Formal Analysis, Investigation, Writing – Original Draft, Writing – Review & Editing, Visualization.

Austin Clark: Conceptualization, Methodology, Software, Data Curation, Formal Analysis, Writing – Original Draft, Writing – Review & Editing, Supervision, Project Administration.

Kent Detrick: Methodology, Validation, Investigation, Data Curation, Writing – Original Draft, Visualization.

Matthew Memmott: Conceptualization, Resources, Writing – Review & Editing, Funding Acquisition.

Stella Nickerson: Writing – Review & Editing, Supervision. Funding Acquisition.

Acknowledgements

This research used resources provided and maintained by the Fulton Supercomputing Laboratory as managed by the Ira A. Fulton College of Engineering and Technology at Brigham Young University, and we gratefully acknowledge this support. We also acknowledge support from the U.S. Department of Energy, Office of Nuclear Energy, Nuclear Energy University Program under Project 19e17413, CID: DENE0008870.

Appendix A

The density apparatus was verified against $(NaNO_3)_{0.3592}(KNO_3)_{0.6408}$ (solar salt). The mixture was chosen for its relatively high melting temperature[61] (~220 °C), the ease of working without the gloveboxes typically required for fluoride salts, and the salt's well documented density values[62]. The literature uses a quadratic model to represent the solar salt density as a function of temperature. However, we found an insignificant quadratic relationship and thus chose a linear model for our predicted densities, as shown in Figure 9. The maximum error in the numerical prediction from a single data point is 0.28%, and the average error in the numerical prediction is 0.09%. The linear model is given in Eq. (9)

$$\rho_{Solar\ Salt}\left[\frac{kg}{m^3}\right] = a + b \cdot T[°C] \qquad (9)$$

where T is temperature, a is 2131.756 ± 1.958 kg/m^3 and b is -0.7339 ± 0.005 kg/(m^3 · °C). Error bounds represent a 95% confidence interval.

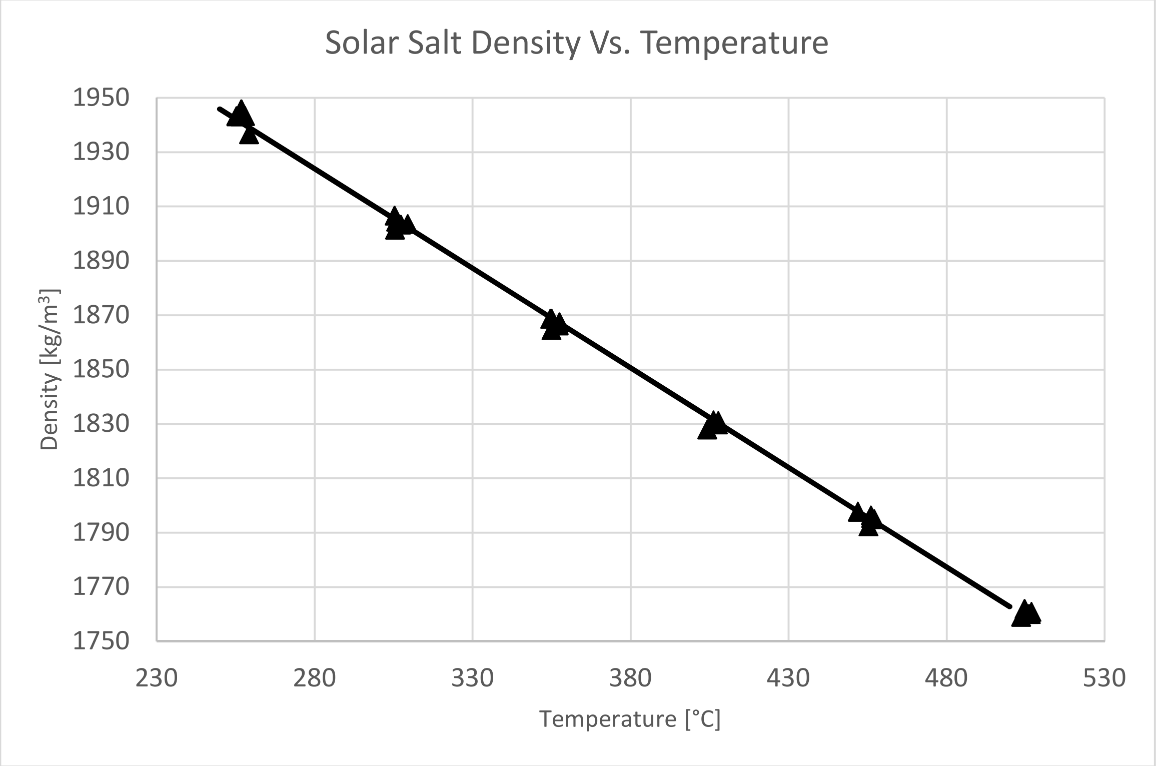

Figure 8: The density of solar salt (kg/m^3) on temperature (°C) for a verification experiment. The equation is a linear fit of the data and the values are given in Eq. 9.

The numerical prediction shown in Figure 8 is plotted against other literature for solar salt in Figure 9. This work is in close agreement with literature values.

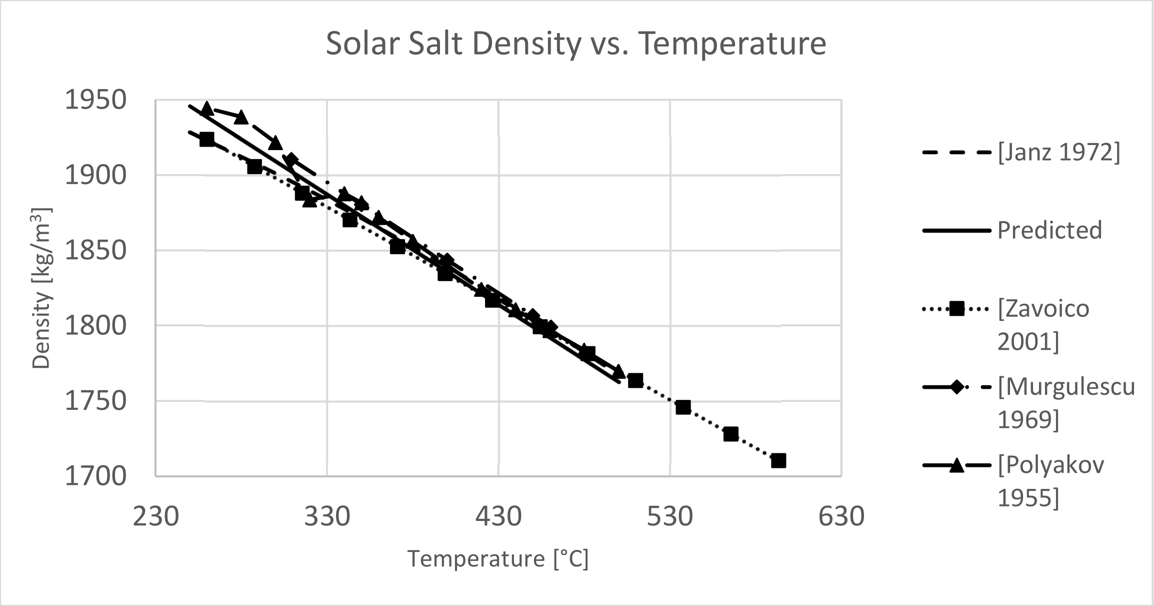

Figure 9: The density of solar salt (kg/m^3) on temperature (°C) contrasting values predicted from our experimental measurements (Eq. 9) and those predicted by literature. Literature predictions are given by Janz et al.[62], Zavoico[63], Murgulescu et al.[64] and Polyakov et al.[65].

As expected, the surface tension and air buoyancy corrections were small when compared to the salt buoyancy force. The force on the bob due to surface tension ($2\gamma\pi D_{wire}$) was about 0.15% of the uncorrected salt buoyancy force ($F_0 - F_1$), The buoyancy force on the bob in atmosphere ($\frac{M_{Ar}P}{RT_0} gV_{probe}(T_0)$) was about 0.06% of the uncorrected salt buoyancy force. These corrections are of similar scale to the error caused by using a linear temperature correlation (again, 0.28% at maximum and 0.09% on average for Eq. 9), and so we take them to be small but significant factory in the determination of molten salt density.

Appendix B

To approximate the additive model, we took a weighted average of the molar volumes for FMgNaK's binary component salts at each temperature. The two resulting points were used to create a simple linear relationship that we used to benchmark our density simulations.

Table 5: Theoretical molar volumes for the additive molar volume approximation by Cantor et. al.[53].

Binary Salt	Molar Volume (cm^3/mol)	
	600 °C	800 °C
NaF	19.08	20.2
KF	28.1	30.0
MgF_2	22.4	23.3

References

1. LeBlanc, D., Molten salt reactors: A new beginning for an old idea. *Nuclear Engineering and Design* **2010,** *240* (6), 1644-1656.
2. Ault, T.; Brozek, K.; Fan, L.; Folsom, M.; Kim, J.; Zeismer, J. *Lithium Isotope Enrichment: Feasible Domestic Enrichment Alternatives*; UCBTH-12-005; University of California, Berkeley: 5 May 2012, 2012.
3. Farrar, K.; Memmott, M., A Consideration of Novel Fuel Carrier Salts in Molten Salt Reactors. *Journal of Nuclear Science and Technology* **Unpublished results**.
4. Kelleher, B. C.; Dolan, K. P.; Brooks, P.; Anderson, M. H.; Sridharan, K., Batch-Scale Hydrofluorination of Li27BeF4 to Support Molten Salt Reactor Development. *Journal of Nuclear Engineering and Radiation Science* **2015,** *1* (4).
5. Yu, H.; Wei, L.; Shengwei, W.; Youshi, Z.; Yuan, Q.; Yulan, L.; Detao, X., Controlling and monitoring of tritium in molten salt reactor. *Nuclear Techniques* **2011,** *34* (8), 632-636.
6. Diamond, D. J. *Phenomena Important in Molten Salt Reactor Simulations*; Brookhaven National Laboratory (BNL): Upton, NY (United States), 2018.
7. 29 C.F.R. § 1910.1024. Occupational Safety and Health Administration: 2018; Vol. Document ID OSHA-2018-0003-0026.
8. Potassium Fluoride. In *LTS Research Laboratories, Inc*, July 01, 2015.
9. Sodium Fluoride. In *Safety Data Sheet UN1690*, LTS Research Laboratories, Inc: July 02, 2015.
10. Magnesium Fluoride. In *Safety Data Sheet*, LTS Research Laboratories, Inc: Sept. 22, 2014.
11. Beryllium Fluoride. In *Safety Data Sheet UN1566*, LTS Research Laboratories, Inc: June 20, 2019.
12. Serp, J.; Allibert, M.; Beneš, O.; Delpech, S.; Feynberg, O.; Ghetta, V.; Heuer, D.; Holcomb, D.; Ignatiev, V.; Kloosterman, J. L.; Luzzi, L.; Merle-Lucotte, E.; Uhlíř, J.; Yoshioka, R.; Zhimin, D., The molten salt reactor (MSR) in generation IV: Overview and perspectives. *Progress in Nuclear Energy* **2014,** *77*, 308-319.
13. Magnusson, J.; Memmott, M.; Munro, T., Review of thermophysical property methods applied to fueled and un-fueled molten salts. *Annals of Nuclear Energy* **2020,** *146*.
14. ForsBerg, W. C. *Molten-Salt-Reactor Technology Gaps*; 2006.
15. Marcus, Y., The compressibility of molten salts. *The Journal of Chemical Thermodynamics* **2013,** *61*, 7-10.
16. Frandsen, B. A.; Nickerson, S. D.; Clark, A. D.; Solano, A.; Baral, R.; Williams, J.; Neuefeind, J.; Memmott, M., The structure of molten FLiNaK. *Journal of Nuclear Materials* **2020,** *537*.
17. Chaleff, E. S.; Antolin, N.; Windl, W.; Blue, T., Ab-Initio Calculation of Spectral Absorption Coefficients in Molten Fluoride Salts with Metal Impurities. *Nuclear Technology* **2018,** *204* (1), 59-65.
18. Bengtson, A.; Nam, H. O.; Saha, S.; Sakidja, R.; Morgan, D., First-principles molecular dynamics modeling of the LiCl–KCl molten salt system. *Computational Materials Science* **2014,** *83*, 362-370.
19. Nam, H. O.; Morgan, D., Redox condition in molten salts and solute behavior: A first-principles molecular dynamics study. *Journal of Nuclear Materials* **2015,** *465*, 224-235.
20. Corradini, D.; Marrocchelli, D.; Madden, P. A.; Salanne, M., The effect of dispersion interactions on the properties of LiF in condensed phases. *J Phys Condens Matter* **2014,** *26* (24), 244103.
21. Heaton, R. B., Richard; Madden, Paul; Salanne, Mathieu; Simon, Christian; Turq, Pierre, A First-principles description of liquid BeF2 and its mixtures with LiF: 1. Potential development and pure BeF2. *Journal of Physical Chemistry B* **2006,** *110*, 11454-11460.
22. Salanne, M.; Simon, C.; Turq, P.; Heaton, R.; Madden, P. A., A First-Principles Description of Liquid BeF2 and Its Mixtures with Lif: 2. Network Formation in LiF-BeF2. *J. Phys. Chem. B* **2006,** *110*, 11461-11467.
23. Salanne, M.; Simon, C.; Turq, P.; Madden, P. A., Heat-transport properties of molten fluorides: Determination from first-principles. *Journal of Fluorine Chemistry* **2009,** *130* (1), 38-44.
24. Gheribi, A. E. C., D.; Dewan, L.; Chartrand, P.; Simon, C.; Madden, P. A.; Salanne, M., Prediction of the thermophysical properties of molten salt fast reactor fuel from first-principles. **2014**.
25. Martinez, J. M.; Martinez, L., Packing Optimization for Automated Generation of Complex System's Initial Configuartions for Molecular Dynamics and Docking. *Journal of Computational Chemistry* **2003,** *24* (7), 819-825.
26. Martinez, L.; Andrade, R.; Birgin, E. G.; Martinez, J. M., PACKMOL: A Package for Building Initial Configurations for Molecular Dynamics Simulations. *Journal of Computational Chemistry* **2009,** *30*, 2157-2164.
27. Hutter, J.; Iannuzzi, M.; Schiffman, F.; VandeVondele, J., CP2K: atomic simulations of condensed matter systems. *Computational Molecular Science* **2014,** *4*, 15-25.
28. Frigo, M.; Johnson, S. G., The Design and Implementation of FFTW3. *Proceedings of the IEEE* **2005,** *93* (2), 216-231.
29. Perdew, J. P.; Burke, K.; Ernzerhof, M., Generalized Gradient Approximation Made Simple. *Physical Review Letters* **1996,** *77* (18), 3865-3868.

30. VandeVondele, J.; Hutter, J., An efficient orbital transformation method for electronic structure calculations. *J Chem Phys* **2003,** *118* (11), 114105.
31. Vandevondele, J.; Krack, M.; Mohamed, F.; Parrinello, M.; Chassaing, T.; Hutter, J., Quickstep: Fast and accurate density functional calculations using a mixed Gaussian and plane waves approach. *Computer Physics Communications* **2005,** *167* (2), 103-128.
32. Lippert, B. G.; Parrinello, J. H.; Michele, A hybrid Gaussian and plane wave density functional scheme. *Molecular Physics* **1997,** *92* (3), 477-488.
33. VandeVondele, J.; Hutter, J., Gaussian basis sets for accurate calculations on molecular systems in gas and condensed phases. *J Chem Phys* **2007,** *127* (11), 114105.
34. Goedecker, S. T., M.; Hutter, J., Separable dual-space Gaussian pseudopotentials. *Physical Review B* **1996,** *54* (3), 1703-1710.
35. Hartwigsen, C.; Goedecker, S.; Hutter, J., Relativistic separable dual-space Gaussian pseudopotentials from H to Rn. *Physical Review B* **1998,** *58* (7), 3641-3662.
36. Krack, M., Pseudopotentials for H to Kr optimized for gradient-corrected exchange-correlation functionals. *Theoretical Chemistry Accounts* **2005,** *114* (1-3), 145-152.
37. Bussi, G.; Donadio, D.; Parrinello, M., Canonical sampling through velocity rescaling. *J Chem Phys* **2007,** *126* (1), 014101.
38. Caro, M. A.; Lopez-Acevedo, O.; Laurila, T., Redox Potentials from Ab Initio Molecular Dynamics and Explicit Entropy Calculations: Application to Transition Metals in Aqueous Solution. *Journal of chemical theory and computation* **2017,** *13* (8), 3432-3441.
39. Shi, R.; Yanting, W., Dual ionic and organic nature of ionic liquids. *Scientific reports* **2016,** *6* (1), 1-12.
40. Zahn, S.; Uhlig, F.; Thar, J.; Spickermann, C.; Kirchner, B., Intermolecular Forces in an Ionic Liquid ([Mmim][Cl]) versus Those in a Typical Salt (NaCl). *Angewandte Chemie* **2008,** *47* (19), 3639-3641.
41. Cantor, S. *Density and viscosity of several molten fluoride mixtures*; ORNL-TM-4308; Department of Energy: Oak Ridge National Laboratory, 1973.
42. Cantor, S.; Cooke, J. W.; Dworkin, A. S.; Robbins, G. D.; Thoma, R. E.; Watson, G. M. *Physical Properties of Molten-Salt Reactor Fuel, Coolant, and Flush Salts*; 1968.
43. Janz, G. J.; Gardner, G. L.; Krebs, U.; Tomkins, R. P. T., Molten Salts: Volume 4, Part 1, Fluorides and Mixtures Electrical Conductance, Density, Viscosity, and Surface Tension Data. *Journal of Physical and Chemical Reference Data* **1974,** *3* (1), 1-115.
44. Janz, G. J.; Tomkins, R. P. T.; Allen, C. B.; Downey, J. R.; Garner, G. L.; Krebs, U.; Singer, S. K., Molten salts: Volume 4, part 2, chlorides and mixtures—electrical conductance, density, viscosity, and surface tension data. *Journal of Physical and Chemical Reference Data* **1975,** *4* (4), 871-1178.
45. Humphrey, W., VMD - Visual Molecular Dynamics. *J. Molec. Graphics* **1996,** *1*, 33-38.
46. Zhang, J.; Forsberg, C. W.; Simpson, M. F.; Guo, S.; Lam, S. T.; Scarlat, R. O.; Carotti, F.; Chan, K. J.; Singh, P. M.; Doniger, W.; Sridharan, K.; Keiser, J. R., Redox potential control in molten salt systems for corrosion mitigation. *Corrosion Science* **2018,** *144*, 44-53.
47. Bloom, H.; Boyd, P. W. D.; Laver, J. L.; Wong, J., Molten salt mixtures. XI. Integral and partial molar volumes in the molten salt systems PbCl2 + NaCl, PbCl2 + RbCl, PbCl2 + CsCl, CdCl2 + RbCl, and CdCl2 + CsCl. *Australian Journal of Chemistry* **1966,** *19* (9), 1591-1596.
48. Bradshaw, R. W. *Effect of composition on the density of multi-component molten nitrate salts*; SAND2009-8221; Sandia National Laboratories: 2009.
49. Delpech, S.; Cabet, C.; Slim, C.; Picard, G. S., Molten fluorides for nuclear applications. *Materials Today* **2010,** *13* (12), 34-41.
50. Sellers, R. S. A. M. H. S., K.; Allen, T. R., Failure analysis of 316L stainless steel crucible by molten fluoride salt interaction with clay bonded silicon carbide. *Engineering Failure Analysis* **2014,** *42*, 38-44.
51. Abdullaev, R. N., Density and Thermal Expansion of High Purity Nickel over the Temperature Range from 150 K to 2030 K. *International Journal of Thermophysics* **2015,** *36* (4), 603-619.
52. Crawley, A. F., Densities of Liquid Metals and Alloys. *International Metallurgical Reviews* **1974,** *19* (1), 32-48.
53. Cantor, S., Estimating Densities of Molten Fluoride Mixtures, in Reactor Chemistry Division Annual Progress Report,. *Oak Ridge National Laboratory* **1966**, 27-29.
54. Song, J.; Shi, S.; Li, X.; Yan, L., First-principles molecular dynamics modeling of UCl3 in LiCl-KCl eutectic. *Journal of Molecular Liquids* **2017,** *234*, 279-286.

55. Nam, H. O.; Bengtson, A.; Vörtler, K.; Saha, S.; Sakidja, R.; Morgan, D., First-principles molecular dynamics modeling of the molten fluoride salt with Cr solute. *Journal of Nuclear Materials* **2014,** *449* (1), 148-157.
56. Marcus, Y., Volumetric behavior of molten salts. *Thermochimica Acta* **2013,** *559*, 111-116.
57. Woodward, C.; Asta, M.; Trinkle, D. R.; Lill, J.; Angioletti-Uberti, S., Ab initiosimulations of molten Ni alloys. *Journal of Applied Physics* **2010,** *107* (11), 113522.
58. Ohno, H.; Furukawa, K.; Takagi, R.; Igarashi, K.; Mochinaga, J., Faraday Transactions 2: Molecular and Chemical Physics. *Journal of the Chemical Society* **1983,** (79), 463-471.
59. Zhang, Y., Electronegativitis of Elements in Valence States and Their Applications. 2. A Scale for Strengths of Lewis Acids. *Inorg Chem* **1982,** *21* (11), 3889-3893.
60. Fitzhugh, R. L.; Clark, A. D.; Nickerson, S. D.; Memmott, M. J.; Harb, J. N., On the Electrochemical Thermodynamics of Minor Components in Molten Salt Mixtures. *Journal of the Electrochemical Society* **2021,** *168* (2), 026502.
61. Romero, M.; González-Aguilar, J., Next generation of liquid metal and other high-performance receiver designs for concentrating solar thermal (CST) central tower systems. In *Advances in Concentrating Solar Thermal Research and Technology*, 2017; pp 129-154.
62. Janz, G. J., ; et al., Molten Salts: Volume 3 Nitrates, Nitrites, and Mixtures: Electrical Conductance, Density, Viscosity, and Surface Tension Data. *Journal of Physical and Chemical Reference Data* **1972,** *1*, 581-746.
63. Zavoico, A. B., Solar Power Tower Design Basis Document. Sandia National Laboratories: Albubquerque, N., Ed. 2001.
64. Murgulescu, I.; Zuca, S., Viscosity of binary mixtures of molten nitrates as a function of ionic radius—II. *Electrochimica Acta* **1969,** *14* (7), 519-526.
65. Polyakov, V.; Beruli, S., Specific weight of alloys from nitrate and nitrite systems of potassium and sodium. *Izvest. Siktora Fiz.-Khim. Anal* **1955,** *26*, 164-172.

Color should be used in print for Figures 2, 3, 4, 6, and 7.